JGR Solid Earth

RESEARCH ARTICLE
10.1029/2021JB022752

Mantle Wedge Seismic Anisotropy and Shear Wave Splitting: Effects of Oblique Subduction

Lindsey M. Kenyon[1] **and Ikuko Wada**[1]

[1]Department of Earth and Environmental Sciences, University of Minnesota, Minneapolis, MN, USA

Key Points:

- In a large portion of the mantle wedge in oblique subduction zones, the olivine crystal preferred orientation (CPO) fast axes do not align with the flow
- The distribution of shear wave splitting parameters is dependent on obliquity, particularly in the forearc and backarc regions
- Fast directions are highly depended on the initial polarization but are mostly margin-normal for A-type and E-type olivine CPO

Supporting Information:

Supporting Information may be found in the online version of this article.

Correspondence to:

L. M. Kenyon,
kenyo099@umn.edu

Citation:

Kenyon, L. M., & Wada, I. (2022). Mantle wedge seismic anisotropy and shear wave splitting: Effects of oblique subduction. *Journal of Geophysical Research: Solid Earth*, *127*, e2021JB022752. https://doi.org/10.1029/2021JB022752

Received 2 JUL 2021
Accepted 28 MAR 2022

Abstract We investigate the evolution of olivine crystal preferred orientation (CPO) and its effect on local shear wave splitting (SWS) in the mantle wedge of oblique subduction zones. Based on model-predicted 3-D mantle wedge flow fields, we compute the A-type and E-type olivine CPO distribution for a range of subduction obliquity. The results show that the seismically fast axis does not necessarily align with the flow direction. To model the local SWS parameter distribution for oblique subduction zones, we apply a full range of initial polarization to multilayer models that approximate the model-predicted CPO distributions. These models result in a bimodal SWS parameter distribution, which relaxes as subduction obliquity increases. Unlike non-oblique subduction models, these models indicate considerable variations in the SWS parameters with subduction obliquity and initial polarization and also among the forearc, arc, and backarc regions. Because of this variability, a single SWS measurement cannot constrain the CPO distribution, and shear waves with a range of initial polarization are required to interpret the SWS parameters in oblique subduction zones. Our results indicate that 3-D mantle wedge flow due to oblique subduction cannot explain commonly observed margin-parallel fast direction in the forearc region but can explain margin-normal fast directions that are observed in the arc and backarc regions of oblique subduction zones.

Plain Language Summary In many subduction zones, the sinking oceanic plate moves obliquely relative to the plate margin, causing 3-D mantle flow in the overlying wedge-shaped region of the mantle. We calculate how olivine crystals become oriented in this 3-D flow for a range of subduction obliquity and examine how the crystal orientation impacts the polarization of shear waves that travel through it. The results show that the relation between the crystal orientation and the flow direction is not uniform in many parts of the mantle wedge. Further, when the crystal orientation varies along the raypath of shear waves, the direction of their fast component and the delay time between the fast and slow components vary significantly with the initial polarization of the shear wave, and the delay time peaks at two different fast directions over the full range of the initial polarization. The distribution of the fast direction and the delay time also vary with obliquity and distance from the margin, but the margin-normal fast direction is dominant in all models and can explain the fast directions that are commonly observed in the arc and backarc of many subduction zones.

1. Introduction

The subduction of oceanic plates induces solid-state flow of the upper mantle in the wedge-shaped region above the subducting plate (Figure 1). The mantle wedge flow brings in hot mantle from the backarc region and is a key factor that affects the thermal structure of the subduction zone and many important processes, such as metamorphic reactions, volatile cycles, arc volcanism, and earthquakes. The pattern of mantle wedge flow and its thermal impact have been quantified using both analytical and numerical models, often assuming a 2-D mantle wedge flow (e.g., Currie et al., 2004; England & Katz, 2010; Furukawa, 1993; Molnar & England, 1990; Syracuse et al., 2010; van Keken et al., 2019, 2002; Wada & Wang, 2009). This assumption is reasonable in some subduction zones where the subduction kinematics and geometry are relatively simple. However, given that mantle wedge flow is driven by mechanical coupling with the subducting plate, its pattern is likely three-dimensional where the subduction direction is not normal to the margin or the slab geometry varies along the margin. Such theoretical predictions have been reported by studies that employ 3-D numerical thermomechanical models (e.g., Bengtson & van Keken, 2012; Jadamec & Billen, 2012; Ji & Yoshioka, 2015; Kneller & van Keken, 2008; Plunder et al., 2018; Wada, 2021; Wada et al., 2015) and analogue models (e.g., Funiciello et al., 2006; Kincaid & Griffiths, 2004; Schellart, 2004). However, the validation of such model predictions remains difficult due to lack of observations that can directly constrain the mantle wedge flow pattern.

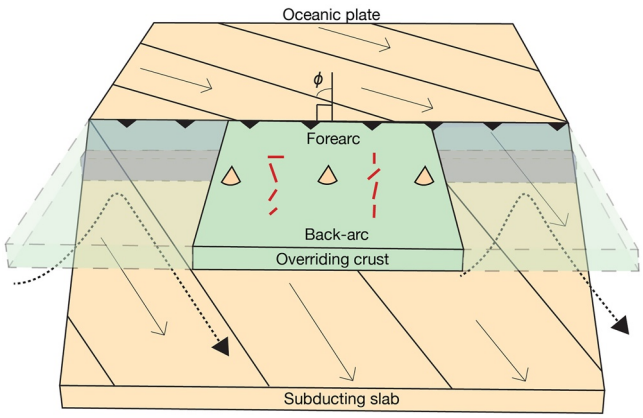

Figure 1. Schematic diagram of a mantle wedge flow pattern (dotted arrows) at an oblique subduction zone, where an oceanic plate (yellow domain) subducts obliquely to the strike-normal axis of the margin. Solid and translucent green domains indicate the overriding crust. Translucent red domain between the overriding crust and the subducting slab indicates stagnant mantle wedge corner. Red thick lines schematically illustrate some possible spatial variations in fast directions from the forearc to the backarc (e.g., Abt et al., 2009). Thin arrows on the incoming and subducting plate indicate the plate motion relative to the overriding plate.

The direction of mantle flow has been inferred indirectly from observations of shear wave splitting (SWS), in which shear waves (*S* waves) become polarized into two orthogonal components that travel at different speeds through an elastically anisotropic medium and thus arrive at a seismic station with some time offset between their arrivals, which is referred to as the delay time (e.g., Christensen, 1984; Savage, 1999; Silver, 1996; Zhang & Karato, 1995). We refer to the polarization direction of the fast component as the fast direction. SWS in the mantle wedge is commonly studied using SKS and local *S* waves. SKS waves originate from teleseismic earthquakes as downgoing *S* waves, which travel through the outer core as *P* waves, reemerge as *S* waves at the core-mantle boundary, and travel up through the entire mantle and through the descending slab before traveling through the mantle wedge (e.g., Greve et al., 2008; Long & Silver, 2008). Local *S* waves originate from earthquakes within the descending slab, traveling through part of the slab before traveling through the mantle wedge (e.g., Long & Wirth, 2013, and references within). The incidence of SKS waves is nearly vertical at recording seismic stations whereas local *S* waves have more variable incidence angles as they may not originate directly below a seismic station. The splitting observations of both SKS and local *S* waves carry information about the elastic properties of the mantle wedge (and the overriding crust), but the former also contains the information on the mantle below the subducting slab.

In the flowing part of the mantle wedge, the primary cause of seismic anisotropy is the alignment of olivine crystals, which are elastically anisotropic. When olivine crystals are oriented randomly, the medium is on average seismically isotropic. However, when the mantle deforms by dislocation creep, olivine crystals become aligned in the crystal preferred orientation (CPO), producing seismic anisotropy. The CPO of olivine depends on the condition and the kinematics of deformation (e.g., simple shear and coaxial), relative activities of different slip systems, and deformation history (Boneh & Skemer, 2014; Skemer et al., 2012). Olivine CPOs due to simple shear are categorized into A–E types. In the A-type, D-type, and E-type CPOs, the *a* axis of olivine is subparallel to the long axis of the finite strain ellipsoid (Skemer & Hansen, 2016). In contrast, in the B-type and C-type CPOs, the olivine *c* axis is subparallel to the long axis of the finite strain ellipsoid, causing the *a* axis to be perpendicular to the flow direction (Karato et al., 2008; Skemer & Hansen, 2016). Additionally, AG-type CPO is found in natural samples and results from coaxial deformation (Michibayashi et al., 2016; Skemer & Hansen, 2016). The conventional approach is to infer the mantle flow direction from the fast direction by assuming a particular type of olivine CPO and that the fast direction indicates the average azimuth of the olivine *a* axis (e.g., Long & Becker, 2010; McPherson et al., 2020; Savage, 1999).

The fast directions that are measured in subduction zones are spatially variable, both within and among subduction zones (Figure 1). However, regardless of subduction obliquity, the fast directions in the forearc and arc regions are more commonly subparallel to the margin than those normal to the margin, and many subduction zones, including oblique subduction zones, exhibit margin-normal fast directions in the backarc (e.g., Abt et al., 2010; Collings et al., 2013; Greve & Savage, 2009; Long & Silver, 2008; Long & Wirth, 2013; Nakajima & Hasegawa, 2004; Richards et al., 2021). Observations of margin-parallel fast directions in the forearc and the arc have been interpreted to indicate margin-parallel mantle flow by assuming A-type olivine CPO (e.g., Hoernle et al., 2008; Long & Silver, 2008). Alternatively, the observations can be explained by margin-normal mantle flow if B-type olivine CPO is invoked (e.g., Kaminski & Okaya, 2018; Kneller & van Keken, 2007). Other possible mechanisms that may cause margin-parallel fast directions include the shape-preferred orientation of melt lenses (e.g., Holtzman et al., 2003) and anisotropy in the overriding crust (e.g., Uchida et al., 2020). The margin-normal fast directions in the backarcs of Alaska and Sumatra have been interpreted to indicate 2-D mantle wedge corner flow based on the assumption that the mantle flow direction is parallel to the fast direction (Collings et al., 2013; Richards et al., 2021). Other studies invoke either more complex flow patterns or other sources of anisotropy for the interpretation of the observed SWS parameters (e.g., Long & Wirth, 2013). Thus, for a given SWS observation, there are varying interpretations of SWS observations across different subduction zones.

Another parameter that is useful in inferring the seismic anisotropic structure of the mantle wedge is the delay time, which indicates the overall effect of the anisotropic medium that *S* waves travel through. The delay time of local *S* waves that travel through the mantle wedge can be relatively long, typically ranging from 0.3 to 1 s, but it can be as long as ∼2 s, indicating a strongly anisotropic medium, given the relatively short distance through the mantle wedge (Long & Wirth, 2013). The long delay times that are observed over the cold nose of the mantle wedge in some forearc regions is difficult to explain by olivine anisotropy given the short raypath through the mantle wedge, requiring other sources of seismic anisotropy, such as the presence of foliated antigorite (e.g., Bezacier et al., 2010; Horn et al., 2020; Katayama et al., 2009; Nagaya et al., 2016; Reynard, 2013) and anisotropy in the overriding crust (e.g., Uchida et al., 2020). In this study, we focus on the effects of olivine CPO on SWS in the flowing part of the mantle wedge where temperature is too high for antigorite to be stable.

Inferring the seismic anisotropy in the mantle wedge from SWS parameters is further complicated by their dependence on the propagation direction and the initial polarization of the *S* waves (Savage, 1999). The propagation direction is described by the back azimuth and the incidence angle of the wave. If the incidence is vertical (0°), then the propagation direction becomes independent of the back azimuth. In the case of SKS waves, the back azimuth determines the initial polarization. This is because there is no energy in the Sh component (*S* wave component in the horizontal plane) upon the wave leaving the core and entering the mantle, and the azimuth of the initial polarization of the Sv waves (component of the *S* wave orthogonal to the Sh component and the propagation direction) is the same as its back azimuth. For local *S* waves, the initial polarization is dependent on the moment tensor of the earthquake. However, polarization of both types of waves are likely modified prior to entering the mantle wedge, given that SKS waves travel through the upper mantle and the subducting lithosphere and local *S* waves travel through part of the subducting lithosphere. Thus, there are generally large uncertainties in the polarization of these waves at the base of the mantle wedge. However, how the uncertainties or the assumptions about the initial polarization affect the interpretation of local SWS observations is unclear.

Numerical geodynamic models have been used to predict the mantle flow pattern and the orientation of olivine *a* axis in subduction zones (e.g., Confal et al., 2018; Faccenda & Capitanio, 2013; Hu et al., 2017; Jadamec, 2016; Jadamec & Billen, 2010; Li et al., 2014; Zhou et al., 2018). Many of the models are relatively large in scale and capture mantle flow patterns both below and above the subducting slab, involving specific tectonic conditions, such as slab edges, slab holes, slab break-off, and slab roll-back. Some of these studies have shown that for complex 3-D mantle flow, the *a* axis of A-type (or D-type or E-type) olivine aligns with the finite strain ellipse (FSE) long axis or the instantaneous strain axis (ISA) and not with the flow velocity vector (e.g., Jadamec & Billen, 2010; Li et al., 2014). SWS parameters have also been calculated based on geodynamic modeling results, many of them assuming SKS splitting (e.g., Confal et al., 2018; Faccenda & Capitanio, 2013; Hu et al., 2017; Zhou et al., 2018). Some numerical modeling studies of subduction focuses on the mantle wedge at a finer resolution using local SWS (Hall et al., 2000; Kaminski & Okaya, 2018; MacDougall et al., 2017), but the effect of 3-D mantle wedge flow pattern due to oblique subduction on local SWS has not been investigated.

Here, we systematically compute local SWS parameters for a range of 3-D mantle wedge flow patterns that result from oblique subduction (Figure 1) and revisit the interpretation of fast direction and delay time. Further, we investigate SWS parameters over a full range of the polarization of the incoming *S* wave at the base of the mantle wedge, which we refer to as the initial polarization (as opposed to the polarization at the mantle-core boundary or at the source of local earthquakes). In this process, we use model-predicted 3-D mantle wedge flow for generic oblique subduction zones with simple slab geometry (Wada, 2021). Using the computed mantle flow field for a given subduction setting, we compute the distribution of average elastic properties of olivine-enstatite aggregates for A-type and E-type olivine CPO in the flowing part of the mantle wedge. We use multiple layers of anisotropic material to approximate the model-predicted distribution of elastic properties in the mantle wedge and compute the local SWS parameters for a full range of initial polarization. The methods and the results of the CPO calculations are presented in Section 2, and those of the SWS calculations are presented in Section 3, followed by discussions in Section 4.

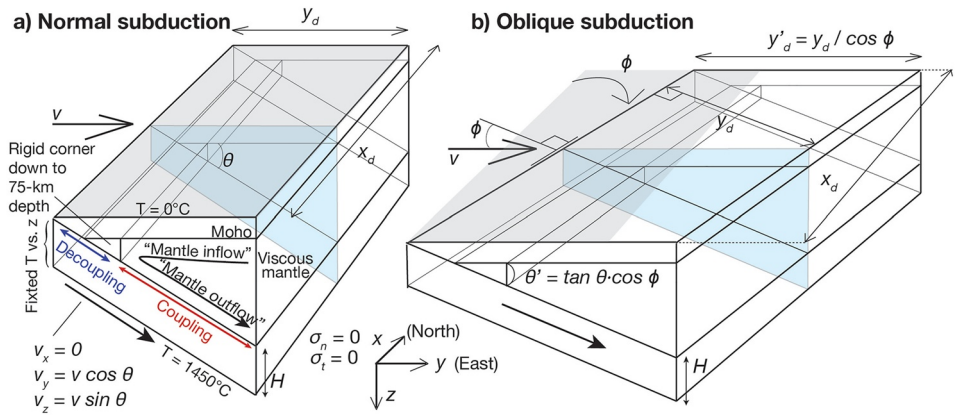

Figure 2. Model set-up for (a) normal subduction and (b) oblique subduction (simplified from Wada (2021)).

2. Distribution of CPO in the Mantle Wedge

2.1. Methods

2.1.1. Mantle Wedge Flow Field

For the mantle wedge flow field, we adopt the results of 3-D numerical models that were developed by Wada (2021) using the finite-element code PGCtherm3D for generic subduction systems. The models were developed to quantify the change in the mantle flow pattern with subduction obliquity. Each model consists of a nondeforming overriding crust, a rigid mantle wedge corner to 75-km depth, a subducting slab with a prescribed motion, and a viscous mantle wedge, in which mantle flow is induced by viscous coupling with the subducting slab (Figure 2). The downdip end of the rigid wedge corner corresponds to the maximum depth of slab-mantle decoupling (MDD), which has been estimated to be 70–80 km for most subduction zones (Syracuse et al., 2010; Wada & Wang, 2009; Figure 2). For the viscous part of the mantle wedge, rheological parameters that are reported for dislocation creep of wet olivine are applied (Hirth & Kohlstedt, 2003).

In all the models that we adopt from Wada (2021), the subducting slab has a planar geometry. For the description of the calculated mantle flow pattern, we treat the positive x axis as north (0°), and the positive y axis as east (90°; Figure 3). The subduction velocity of 5 cm/yr is imposed due east, and oblique subduction is simulated by rotating the orientation of the strike of the trench. Thus, the trench-side vertical boundary is rotated clockwise by a specified amount of obliquity (ϕ) while the subduction direction is kept due east. In all cases, the backarc vertical boundary is placed at a 150-km margin-normal distance from the horizontal location of the MDD. The model length in the x direction is 600 km in all cases. The model width in the y direction and the maximum depth of the slab surface vary with subduction obliquity and slab dip (θ). The geotherm that is applied on the trench-side vertical boundary is calculated by using the GDH1 plate cooling model (Stein & Stein, 1992) for a 30-Ma slab, and the geotherm on the backarc-side vertical boundary is calculated by assuming a surface heat flow of 80 mW m^{-2}, a mantle potential temperature of 1,350 °C, and an adiabatic temperature gradient of 0.3 °C.

In Wada (2021), the subduction obliquity and the slab dip were varied to test their effects on the mantle flow patterns. We use a model naming convention where S denotes "subduction" with the first numeral indicating the degree of subduction obliquity and the second indicating the dip angle (Table S1 in Supporting Information S1). In the model with 0° obliquity and 45° dip (Model S0-45), the azimuthal mantle inflow and outflow directions are parallel to the subduction direction, resulting in a two-dimensional flow pattern (Figures 3a and 4a). In the models with 30° and 45° obliquities (Models S30-45 and S45-45, respectively), the mantle flows in from the southeast quadrant, with a small updip component as in the 0° obliquity model and flows out toward the east parallel to the motion of the subducting slab (Figure 3). With increasing obliquity, the azimuthal angle between the inflow and the outflow increases, and in the model with 60° obliquity (Model S60-45), the mantle flows in approximately from south.

In this study, for the analyses of flow velocities and CPO, we take a vertical cross-section parallel to the subduction direction through the center of each model (Figure 4). In the cross-section, we distinguish the regions of

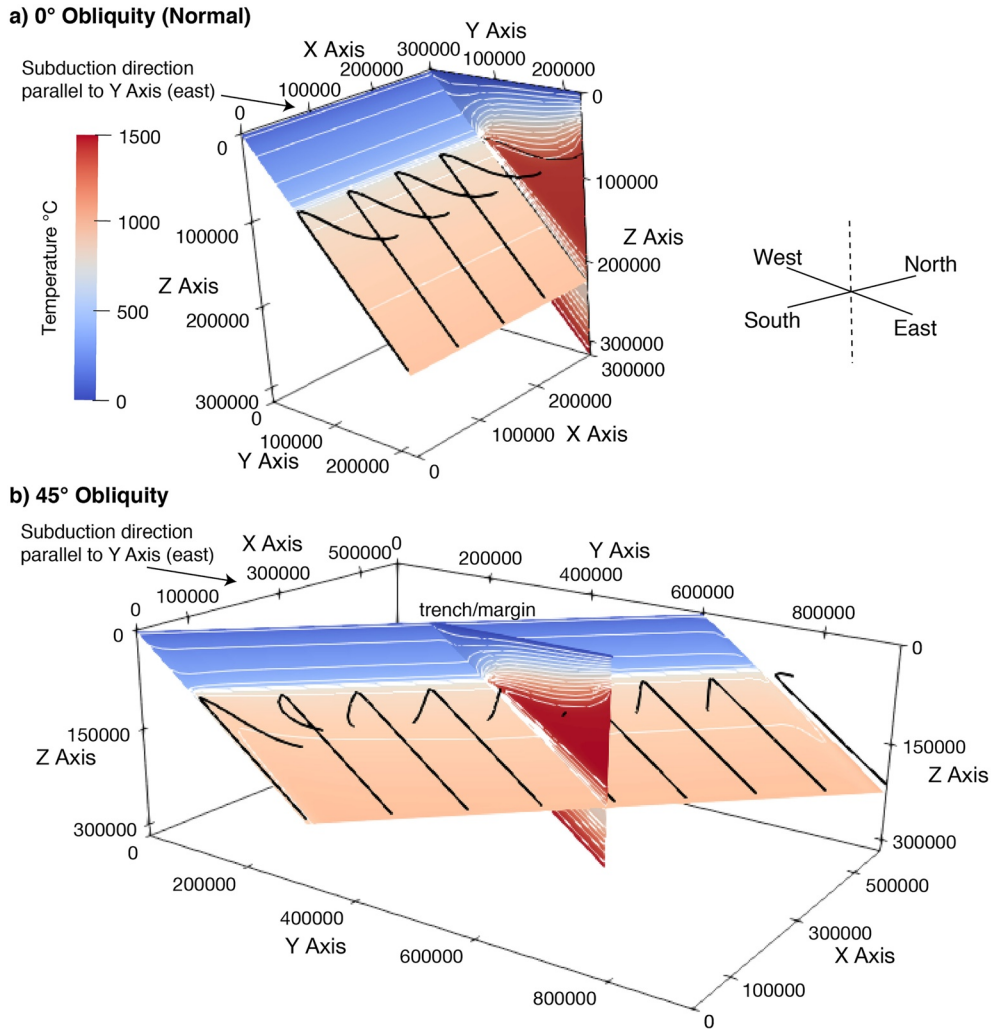

Figure 3. 3-D view of the mantle flow streamlines (thick black lines) and the slab surface temperature (color) for (a) a normal subduction zone with 45° dip (Model S0-45) and (b) subduction zone with 45° obliquity and 45° dip (Model S45-45). Thin white lines indicate temperature contours at every 100 °C.

inflow and outflow based on the consistency in the azimuth of flow vectors. For oblique subduction models, the change in the flow direction is gradual over a relatively narrow region between the inflow to outflow regions. We refer to this narrow region as the transition region. The outflow region at the bottom of the wedge grows in thickness with increasing depth. At a given depth, the horizontal widths of the transition region and the outflow region (purple and clear areas, respectively, in the lower panels of Figures 4b–4d) increase with subduction obliquity. Increasing the dip of the model results in a larger vertical component and a reduced horizontal component of both the inflow and the outflow velocities (Figure S1 in Supporting Information S1). The thickness of the lithosphere in the overriding plate also increases with increasing dip of the slab. The azimuthal direction of the flow and thus the azimuthal angle between inflow and outflow are generally unchanged with the slab dip.

2.1.2. Calculating Anisotropic Elasticity Tensors for the Mantle Wedge

We use D-Rex, a code for calculating CPO and anisotropic elasticity tensors for a given velocity field (Kaminski et al., 2004). D-Rex calculates accumulated strain along a streamline, assuming dislocation creep, dynamic recrystallization and grain boundary migration as mechanisms for the CPO development, and it can incorporate the effect of a secondary phase, such as enstatite. In D-Rex, the dynamics of CPO development are controlled by three parameters, λ^*, M^*, and χ, which represent the nucleation parameter, "intrinsic" grain boundary mobility, and a threshold "dimensionless" volume fraction for the activation of grain boundary sliding, respectively

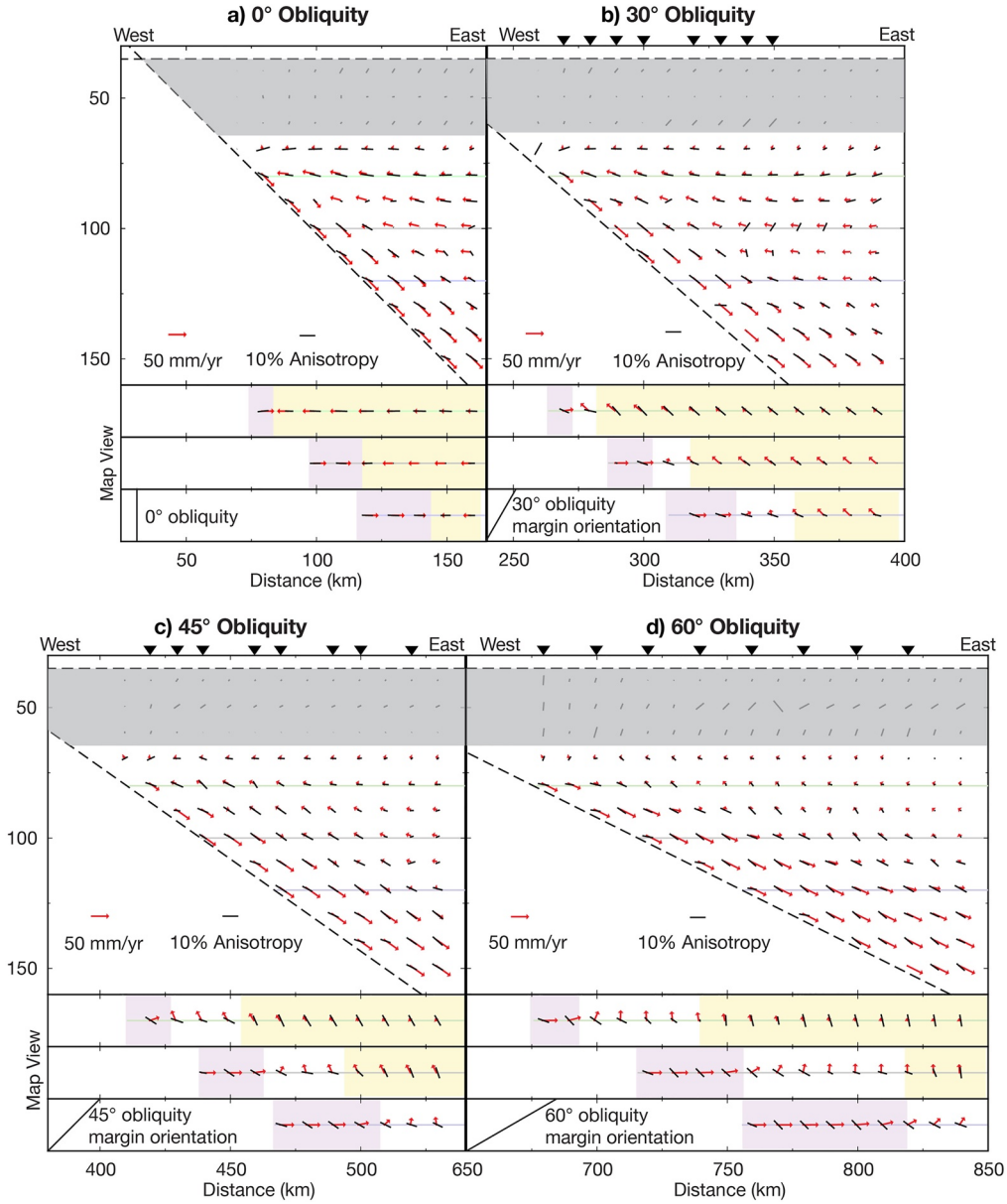

Figure 4. (a–d) Velocity vector (red arrows) and average transverse isotropy (TI) axis (black bars) projected onto a vertical plane (top panel) and horizontal planes (bottom three panels) at the depths of 80, 100, and 120 km for models with 0°, 30°, 45°, and 60° obliquity (Models S0-45, S30-45, S45-45, and S60-45), respectively. The overriding lithosphere, approximated by the shallow region with negligible velocities, is shaded gray. The TI axis is calculated for A-type olivine crystal preferred orientation (CPO). As 3-D vectors are projected onto a plane, the vectors in the top panels indicate only the vertical and E-W components of the full vectors, and those in the lower panels indicate only horizontal components; short vectors in a given panel do not necessarily indicate small magnitudes of the full vector. Inverted triangles at the top indicate the columns for which shear wave splitting (SWS) calculations are performed and presented in Figures 7 and 8.

(Kaminski et al., 2004). These parameters are calibrated with experimental results on the CPO development and deformation of olivine aggregates. Laboratory experiments and CPO models indicate that minerals with and without preexisting textures that are subjected to the same deformation condition exhibit different mineral fabrics and that M* is 125 ± 75 for minerals without preexisting textures (Kaminski et al., 2004) and ~10 for those with preexisting textures (Boneh et al., 2015). The deformation history prior to the material entering into the region of our interest can impact the calculated CPO, but choosing a preexisting texture requires further assumptions of backarc mantle dynamics and assessing these assumptions are beyond the scope of this study. Given these

uncertainties and that the relatively large strain that occurs within our study region likely overrides the previous CPO, we choose to start with random crystal orientations and use an M* value of 125. We use values of 5 for λ* and 0.3 for χ in agreement with both Boneh et al. (2015) and Kaminski et al. (2004). The single crystal elastic moduli for olivine and enstatite are listed in Table S2 in Supporting Information S1. In each D-Rex calculation, we use 1,000 crystals that consist of 70% olivine and 30% enstatite. The reference resolved shear stresses that are used in the calculations of elasticity tensors for A-type and E-type olivine are listed in Table S3 in Supporting Information S1 and example plots of the percent anisotropy for the resulting elastic tensor output for both A-type and E-type resolved stresses are shown in Figure S2 in Supporting Information S1.

We calculate the CPO and elastic tensors on a 10-km by 10-km grid (CPO grid) along the vertical cross-section parallel to the subduction direction through each of the 3-D mantle flow fields discussed in Section 2.1.1 (Figure 4). The CPO and the elastic tensor at each node on the CPO grid are calculated based on the 3-D streamlines and the strain history that are calculated from the velocity and the velocity gradient on a 3-D velocity grid that is spaced 10-km by 1-km by 1-km in the x, y, and z directions, respectively (Text S1 in Supporting Information S1). The upstream calculation is terminated when one of the following three criteria is met: (a) the total strain reaches 10, (b) the total time lapsed reaches 5 million years, and (c) the streamline crosses the backarc-side vertical boundary of the 3-D flow field. The second criterion is most relevant in the lithosphere where the strain rate is very low and thus it takes an unreasonably long time to meet the first criterion. For each node, D-Rex calculates the full elastic tensor and also a hexagonally symmetric tensor that best approximates the full elastic tensor. In visualizing the CPO, the symmetry axis of the best fit hexagonal tensor, hereafter referred to as the transverse isotropy (TI) axis, is used to represent the average fast axis of the aggregate.

2.2. Results of CPO Calculations

When A-type olivine CPO is assumed and the subduction direction is normal to the margin, the azimuthal direction of the TI axis generally aligns with the flow direction, consistent with the common assumption (Figure 4a). However, the plunge of the TI axis deviates from that of the flow vector except in the shallowest part of the inflow region. The plunge difference in the outflow region is relatively small but occurs broadly. This is likely due to the low strain rate in the cold, highly viscous outflowing part of the mantle, causing slow CPO evolution and the downdip propagation of the difference in the plunge angle between the TI axis and the flow vector. The plunge difference in the deeper part of the inflow region is large, and this is likely caused by the variation in the plunge of the flow vectors along the streamline. The deviation of the TI axis orientation from the flow direction could be even larger if the smaller grain boundary mobility M* of 10 is used as the CPO evolution would be slower.

In oblique subduction models with A-type olivine CPO, the azimuthal alignment of the TI axis with the flow direction varies between the inflow, outflow, and transition regions. The TI axis in the inflow region generally aligns with the flow vector in map view (light yellow regions in the lower panels of Figures 4b–4d). However, there is a noticeable difference in their azimuths in the transition zone, where the flow direction changes rapidly, due to the changing flow direction along the streamline. The magnitude of azimuthal angle offset is similar for all oblique subduction models, but the width of the transition region where the offset is predicted increases with increasing subduction obliquity (e.g., ~0.3 and ~0.5 normalized distance for 30° and 60° obliquities, respectively; Figure 5). In the outflow region, the difference remains relatively large, particularly for larger obliquities and close to the transition region, but it decreases toward the base of the mantle wedge. The difference in the plunge angle between the TI axis and the flow vector follows the same pattern as in the normal subduction model as described above.

Models with different slab dips but the same obliquity indicate the same general pattern of the TI axis orientation relative to the flow vector. In models with larger dip angles, due to geometrical effects, the TI axis plunges more steeply in both the inflow and outflow regions to be more compatible with the flow vector (Figure S1 in Supporting Information S1).

With E-type olivine CPO, the pattern in the variation of the TI axis relative to the flow direction is comparable to A-type CPO (Figure S3 in Supporting Information S1). The azimuth of the TI axis generally follows the flow direction in the inflow region and the deeper part of the outflow region but deviates from the flow direction in and near the transition region, as described for A-type CPO. The plunge of the TI axis also follows the same pattern as in the normal and oblique subduction models with the A-type CPO.

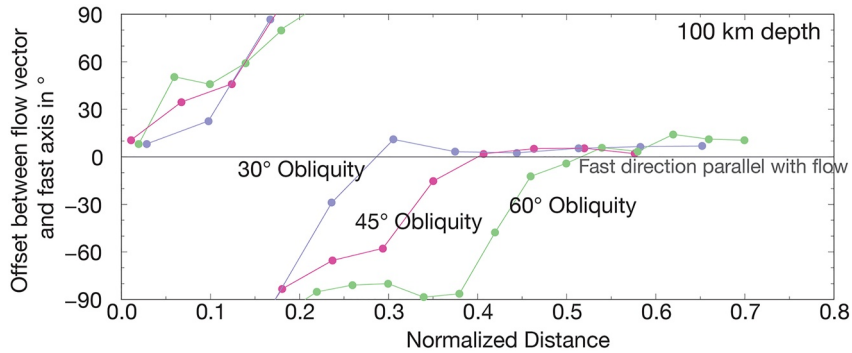

Figure 5. Azimuthal offset between the mantle flow vector and the average transverse isotropy (TI) axis plotted against the horizontal distance that is normalized to the distance from the slab surface to the edge of the subduction model at 100-km depth for each model.

3. Shear Wave Splitting

3.1. Methods

We choose eight horizontal sampling locations that are spread out from the forearc to the backarc region and divide each vertical column through the mantle wedge into 10-km-thick horizontal anisotropic layers, each with a uniform elasticity tensor. We compute SWS parameters for each column, using a SWS code (Kenyon and Wada, 2022), which is built on the MATLAB Seismic Anisotropy Toolkit (MSAT) for seismic and elastic anisotropy (Walker & Wookey, 2012) with the Gaussian wavelet method, based on the ray theory approach for splitting parameter calculations (Bonnin et al., 2012). The choice of the sampling locations and therefore the placement of the layers affect the exact orientations of the fast axes in a given column and the outcome of the SWS calculations. What is being assumed here is that the variation in the fast axis orientation within the given layer is relatively small. Modeling results (not shown) indicate that discretizing the vertical column into thinner layers does not change the overall pattern of the SWS parameter distributions significantly, and therefore the variation in the elastic tensor within a given layer is indeed expected to be relatively small. The calculations are performed for layers with sufficient anisotropy, which is quantified based on the ratio of the slow component (Vs_2) to the fast component (Vs_1) of the *S* waves. We exclude layers with $Vs_2/Vs_1 > 0.99$ ($Vs_1 \approx Vs_2$) in the splitting calculations. All layers where we find $Vs_1 \approx Vs_2$ are located in the lithosphere (gray shaded areas noted in Figure 4). We also neglect any impact of "frozen-in" anisotropy in the lithosphere. We use a relatively high frequency of 0.5 Hz, suitable for local *S* waves (Long & Wirth, 2013).

In the studies of seismic anisotropy, elasticity tensors of the mantle material are commonly assumed to be of hexagonal or orthorhombic symmetry (e.g., Abt & Fischer, 2008; Becker et al., 2006). Although the elasticity tensor for single crystal olivine is indeed orthorhombic (Figure 6; Browaeys & Chevrot, 2004), the elasticity tensor for an aggregate of olivine and enstatite crystals contains more complex symmetries than hexagonal or orthorhombic. The impact of simplifying the tensor symmetry can be investigated by decomposing the tensor into several symmetry classes (e.g., Browaeys & Chevrot, 2004), and the full tensor and its best fit hexagonal approximation, for example, can have notably different maximum percent anisotropy. In this study, we choose to use the full tensor calculated by D-Rex in Section 2 for each layer.

With the MSAT toolbox and the Gaussian wavelet method, a wavelet with initially linear particle motion is split as it encounters and travels through an anisotropic layer. The resulting particle motion at the surface is used to determine the fast direction and delay time for the whole path (Figure S4 in Supporting Information S1). If the particle motion at the surface is linear, it indicates that the material underneath is isotropic and the wave was not split. In this case the covariance matrix of the two components of the wavelet has one eigenvalue. If the particle motion at the surface is nonlinear, it indicates that the material underneath is anisotropic and the covariance matrix from the two components of the split wavelet has two eigenvalues. From the nonlinear particle motion, the initial linear particle motion can be recovered in an ideal situation by Silver and Chan's (1991) method of minimizing the second eigenvalue. This is equivalent to removing and thus identifying the overall impact of the SWS as a result of the anisotropic medium, and the impact is described by a fast direction and a delay time. By applying

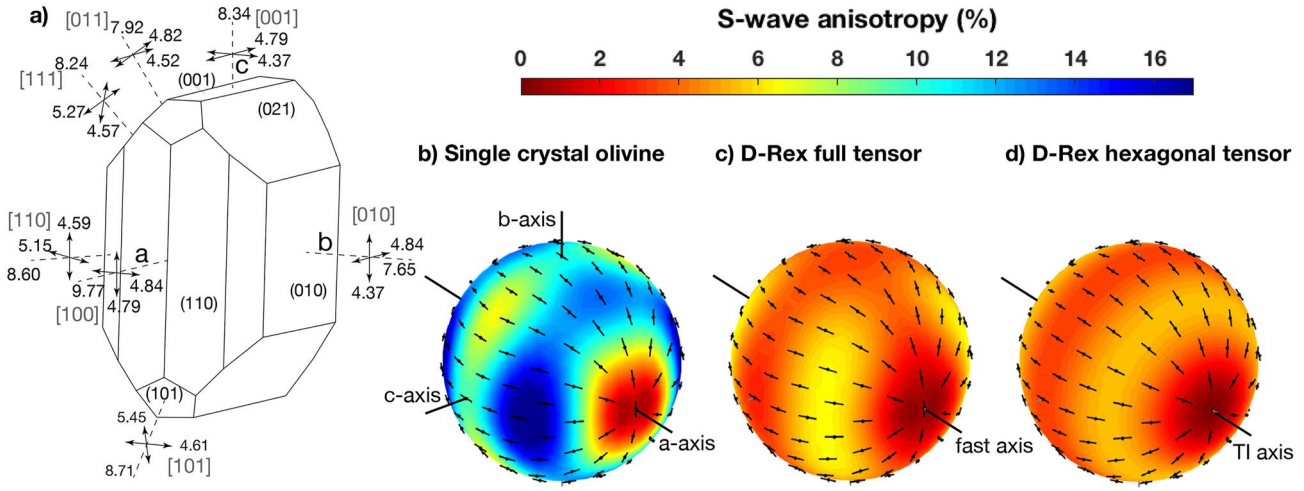

Figure 6. (a) *P* wave velocities (values for the dashed lines) and the fast and slow components of *S* wave velocities (values for double-headed arrows) in km/s through an olivine crystal that are calculated by using the elastic moduli from Abramson et al. (1997), and fast direction (thin black bars) overlain on *S* wave anisotropy (color) for (b) a single crystal olivine and (c) a D-Rex full elastic tensor for an aggregate of 70% olivine and 30% enstatite and (d) the hexagonal approximation to the tensor in (c). The olivine crystal outline in (a) is from Babuska and Cara (1991).

this approach to constrain the SWS parameters for a medium that consists of multiple anisotropic layers, as in real solid Earth, the overall impact of the anisotropic medium is represented by a single set of splitting parameters as if the entire medium was uniformly anisotropic. Due to this assumption, the fast direction from a single SWS measurement does not reflect the anisotropic property of any particular one of the layers that constitute the medium.

Further, applying the Silver and Chan's (1991) eigenvalue minimization method, which assumes a single set of SWS parameters, to an anisotropic medium with two or more layers is known to result in overestimation of delay times and is further impacted by inadvertent time shifting of the wavelets by a half-wavelength, whose consequence is referred to as "cycle skipping" (Rümpker & Silver, 1998; Walsh et al., 2013). There are other approaches to constraining the splitting parameters, such as the cross-convolution method (e.g., Menke & Levin, 2003) and the splitting intensity method (e.g., Chevrot, 2000), but the approach that we adopt here has been widely used in forward modeling studies (e.g., MacDougall et al., 2017) and in subduction zones SWS studies (e.g., Wirth & Long, 2010).

The effects of the *a* axis orientation, percent olivine and enstatite, and the incidence angle on SWS parameters in one-layers and two-layers models have been examined and described in Text S2 in Supporting Information S1, and the resulting SWS parameters are summarized in Tables S4 and S5 and plotted in Figures S5–S8 in Supporting Information S1. To present the calculated SWS parameters for all SWS models, we use azimuth polar plots, indicating the distribution of the fast direction with the delay time for the full range of initial polarization (Figure 7 and Figures S5–S10 in Supporting Information S1). These plots are neither rose plots that bin the data by counts nor lower hemisphere projections that are often used to plot SWS results in seismic studies.

The particle motion at the surface depends on the initial polarization direction of the wavelet. Using multilayer models, we test the effect of the initial polarization direction over its full $\pi/2$ (90°) range at a one-degree interval. This results in the periodicity of the SWS parameters of $\pi/2$. This periodicity of SWS parameters with the initial polarization is different from the periodicity of the fast direction, which is always π, resulting in a pattern of fast directions on an azimuthal polar plot that is antisymmetric about an axis whose orientation depends on the anisotropy of the medium (Figure 7). Nonvertical incidence results further in the dependence of the SWS parameters on the back azimuth of the wave (Text S2 in Supporting Information S1). Given the complex variations in the SWS parameters with incidence angles, we use vertical incidence, focusing on the effects of subduction obliquity and initial polarization without the impact of back azimuth. However, a small incidence angle (<10°) would not change the results significantly (Text S2 in Supporting Information S1).

10.1029/2021JB022752

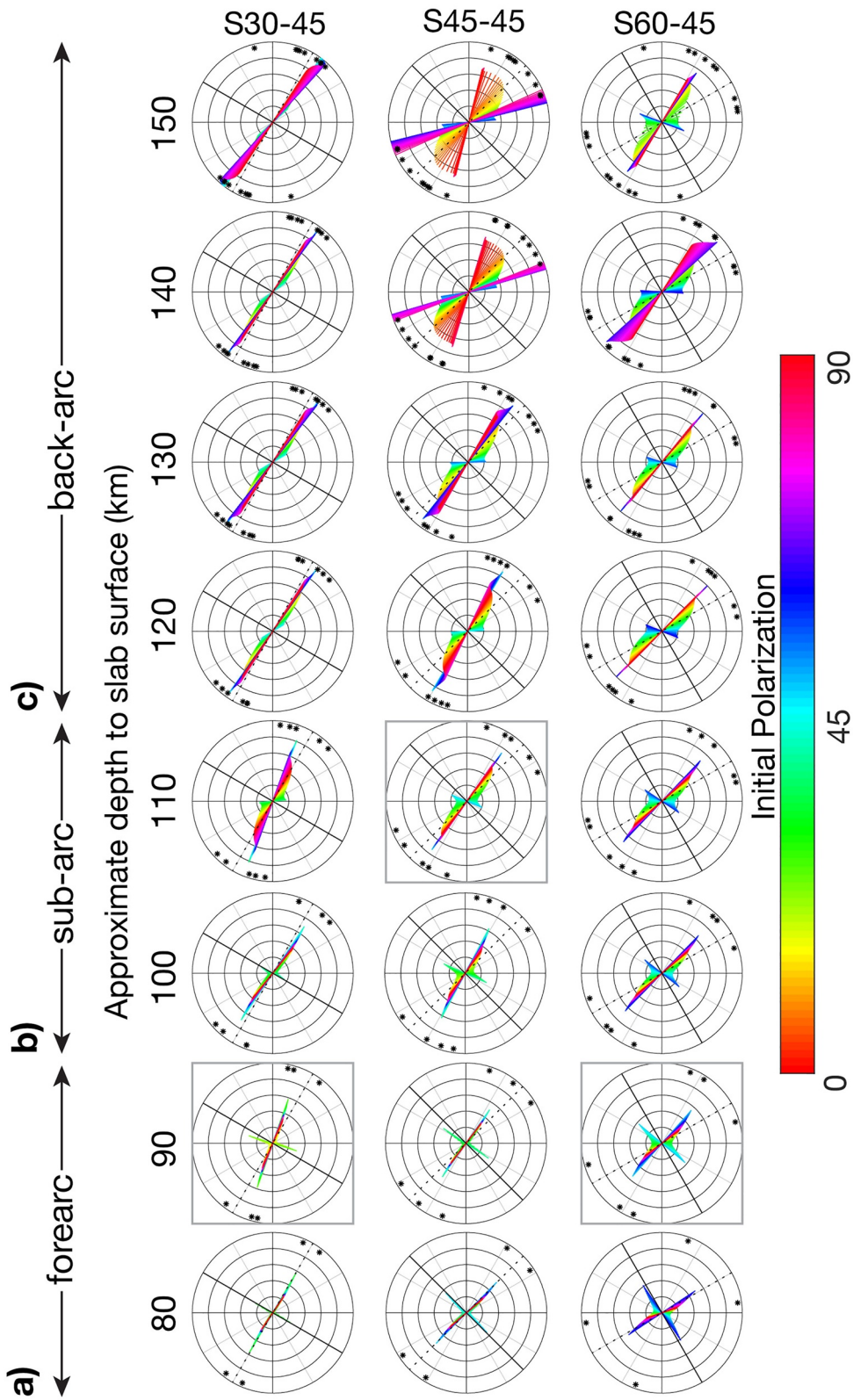

Figure 7. Azimuth polar plots showing shear wave splitting (SWS) parameter variation with depth to the slab surface and subduction obliquity for A-type olivine in the (a) forearc, (b) arc, and (c) backarc on the previous page with gray boxes indicating the plots highlighted in (d) above. The features of the plot that are discussed in the text are labeled in the center plot in (d). The radius indicates the delay time, the azimuth indicates the fast direction, and the color indicates the initial polarization. Asterisk indicates the fast direction that results from traveling vertically through each anisotropic layer independently. Locations of columns within the mantle wedge are indicated in Figure 4. In (d), the left plot exhibits tight bimodal SWS parameters, the center plot shows a relaxed bimodal SWS parameters, and the right plot shows a skewed ribbon-like distribution that is no longer bimodal and characterized by off-peak delay times that are similar to or longer than secondary peak delay time (SDT).

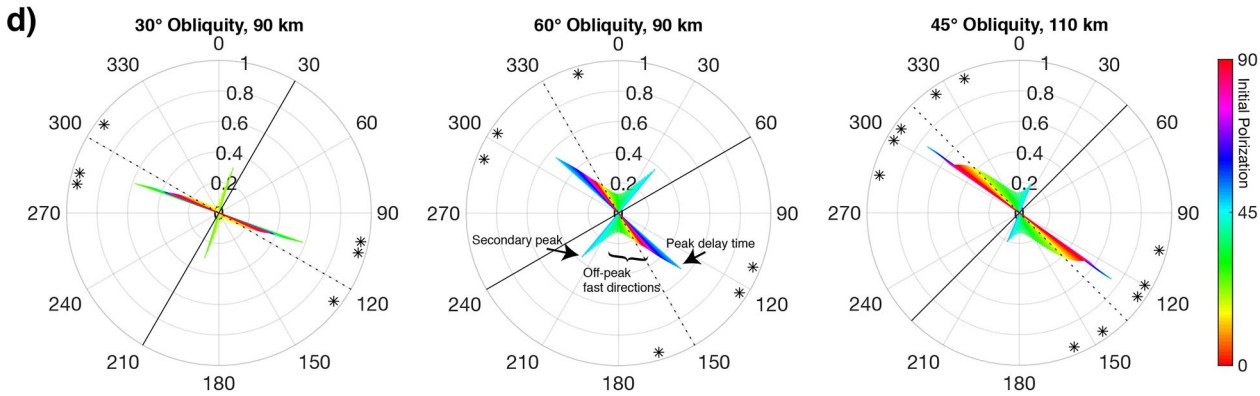

Figure 7. (Continued)

3.2. Results of SWS Calculations

Across all obliquities and slab depths, the pattern of variations in the SWS parameters are similar for both A-type and E-type olivine CPO when vertical incidence is used (Figures 7 and S10 in Supporting Information S1). Given the similarity between the two olivine CPOs, we focus our discussion on A-type CPO. However, the delay time can be longer for E-type olivine, particularly if the *a* axis is plunged by 30–45° as shown by the one-layer models (Figures S5 and S6 in Supporting Information S1).

In the following, we describe the pattern of variations in the SWS parameters with initial polarization, subduction obliquity, and the location relative to the arc, using the following characteristics: (a) the bimodality of the distribution of the fast direction and (b) the fast directions with the peak delay time (PDT) and the secondary peak delay time (SDT; Figure 7d). A bimodal distribution of the fast direction refers to those in which the delay time is negligibly small except for those around the PDT and SDT fast directions. Long off-peak delay times result in a relaxed bimodal distribution or a skewed ribbon-like distribution. As discussed in Section 3.1, using the Silver and Chan's (1991) approach can result in overestimation of the delay times and therefore PDT and SDT that are longer than the sum of the maximum delay times of all layers due to cycle skipping, requiring some caution in relating the delay times to the amount of anisotropy present. However, the distribution of the SWS parameters is still useful in constraining the anisotropic structure (e.g., Aragon et al., 2017), particularly when the initial polarization is spread over a wide range.

There is considerable variation in the pattern of the SWS parameters among the forearc, arc and backarc regions, and the spatial variability also varies with subduction obliquity (Figure 7). Overall, our SWS modeling results indicate that the fast direction is predominantly margin-normal although some initial polarizations do result in margin-parallel and margin-oblique fast directions (Figures 7 and 8).

In the forearc region, beneath which the slab surface lies at 70–90 km depth, the distribution of the fast direction is bimodal, and the PDT and SDT fast directions are nearly perpendicular and parallel to the margin, respectively, for all obliquities, resulting in a fast direction range of ~90° (Figure 7a). Models that consist of just two anisotropic layers indicate that the bimodal distribution becomes more prominent when the two layers contribute unevenly to SWS (e.g., the layer thickness or the anisotropy strength are unevenly distributed, Text S2 and Figures S8a–S8b, S8d–S8e in Supporting Information S1) or when the fast axis in the top or bottom layer is steeply plunged, effectively reducing the azimuthal anisotropy (Figure S8j in Supporting Information S1). The tight bimodal distribution in the forearc region (and elsewhere), therefore, may be indicative of uneven contributions from different layers, such as the inflow and outflow regions. The off-peak delay times at low obliquities are very small (<0.1 s) and may not be large enough to be resolved by SWS observation, potentially limiting the observed fast directions to perpendicular and parallel to the margin in the forearc. The bimodal distribution becomes more relaxed with increasing obliquity as the PDT decreases and the off-peak delay times increase (Figure 7). A wider range of initial polarizations results in the margin-normal fast direction than in the margin-parallel fast direction, and therefore the margin-normal fast direction should be more dominant if initial polarization is randomly distributed. If the initial polarization is biased in a particular direction, it will determine

whether the observed fast direction is perpendicular or parallel to the margin, making the initial polarization a critical factor.

In the arc region, beneath which the slab is at depths of 100–110 km, the PDT fast direction is less dependent on the subduction obliquity than the forearc and varies by only ~25° among models with different subduction obliquities, and all are approximately margin-normal (Figure 7b). The SDT fast direction is 80°–90° from the PDT fast direction. With increasing slab depth and wedge thickness, the SDT decreases while the PDT increases, resulting in a relatively large difference between PDT and SDT. Compared to the forearc region, the off-peak delay times are longer, and the bimodal distribution is more relaxed, resulting in a ribbon-like distribution in some cases (Figures 7b, 110 km slab depth). With increasing obliquity, the off-peak delay times increase, but the increase in PDT and the decrease in SDT with slab depth are less pronounced. However, SDT and off-peak delay times are relatively short, and they result from a relatively narrow range of initial polarizations. Thus, their measurements may potentially become overshadowed by measurements of PDT and near-PDT fast directions, which are within ~15° of the margin-normal axis for all obliquities. The range of fast directions narrows from ~90° to ~60°–80° with increasing depth for all obliquities. The overall pattern of fast direction and delay time in the arc region is remarkably similar to the ones observed in the two-layer models (Text S2 in Supporting Information S1) with 30–60° *a* axis azimuthal offset, and thus two-layer models with horizontal anisotropy may provide a reasonable approximation to the subarc mantle. For regions with sufficient observations, potentially with a range of initial polarizations, such as in NE Japan (e.g., Uchida et al., 2020), the characteristics of the two layers may be constrained based on the SWS parameter distribution; a similar approach has been applied for resolving mantle anisotropy in other tectonic settings (for example, beneath the central Appalachians by Aragon et al. (2017)).

In the backarc region, beneath which the slab reaches a depth of 120–150 km, the delay times are less bimodal, more ribbon-like, and the SDT is smaller than that for the forearc or arc regions for all obliquities (Figure 7c). The distribution of the SWS parameters in the backarc is notably different from those in the forearc and arc regions. The angle between the PDT and SDT fast directions is highly variable, depending on the subduction obliquity, whereas the SDT fast direction is nearly perpendicular to the PDT fast direction in the forearc and arc regions. The SDT disappears completely for 30° obliquity in the backarc region. Where present, the SDT fast direction is no longer margin-parallel and is generally margin-oblique. The range of fast directions increases with obliquity: from ~20° for 30° obliquity to ~80° for 60° obliquity. The fast directions in the backarc for all obliquities are margin-normal to margin-oblique (with two exceptions in E-type results, but it does not appear systematic; Figure S10 in Supporting Information S1). The delay times generally range from ~0.2 s to longer than 1 s (e.g., PDT for 30° obliquity). At the backarc locations with slab depths of 140–150 km, the 45° obliquity models have relatively long (>1 s) PDT and delay times with similar fast directions that are oblique to the margin. These delay times are likely overestimated due to cycle skipping (Text S2 and Figures S9c and S9d in Supporting Information S1).

At all slab depths, an increase in obliquity leads to a more relaxed bimodal distribution with longer off-peak delay times. A similar trend is observed in the two-layer models with increasing offset between the *a* axes of the two layers (Text S2 in Supporting Information S1). These modeling results indicate that observable fast directions (i.e., those with measurable delay times) tend to be limited to either margin-normal or margin-parallel in subduction zones with little obliquity. With increasing obliquity, there is likely more variation in observable fast directions. Comparison between SWS observations at a given station and the SWS parameter distributions that are presented here should provide the sense of the range of initial polarization and the significance of individual measurements. However, the direct comparison to observations may be difficult when the results of observations are expressed using a rose diagram, for which the radius indicates the number of measurements in the respective fast direction bin instead of the delay time.

There is no clear systematic variation in SWS parameter results from variation in the slab dip. The fast directions and delay times are not strongly dependent on the plunges of the fast axes of the layers as long as the plunges are no greater than 60° (Text S2 and Figure S1 in Supporting Information S1). If the fast axis is plunged steeply in any of the layers, such as above a steeply dipping slab, the azimuthal anisotropy would be weak, and it would not contribute significantly to SWS.

Although the PDT fast direction is generally close to margin-normal across the system, depending on the initial polarization (and the back azimuth for nonvertical incidence), the fast direction can vary by up to ~90°, and the delay time can also vary from null to ~1 s. The potential range of variation in the SWS parameters from forearc to backarc is illustrated in Figure 8 by assuming a given initial polarization and near vertical incidence of incoming *S* waves at all observation locations. For normal subduction, the fast direction is margin-normal, independent of the initial polarization, and the delay time increases from the forearc to the backarc as expected (Figure 8a). For oblique subduction, the fast direction is also largely normal to the margin, and the delay time generally increases from the forearc to the backarc with some exceptions.

In the forearc region of oblique models, there are some margin-parallel fast directions with a relatively short delay time (Figure 8). As in most other cases, the margin-parallel fast direction falls close to the SDT fast direction, and thus the delay times for the margin-parallel fast directions are generally shorter than the delay times for margin-normal fast directions. Only Model S60-45, with the greatest obliquity, shows margin-oblique fast directions in the forearc, but these fast directions are off-peak fast directions and thus have very

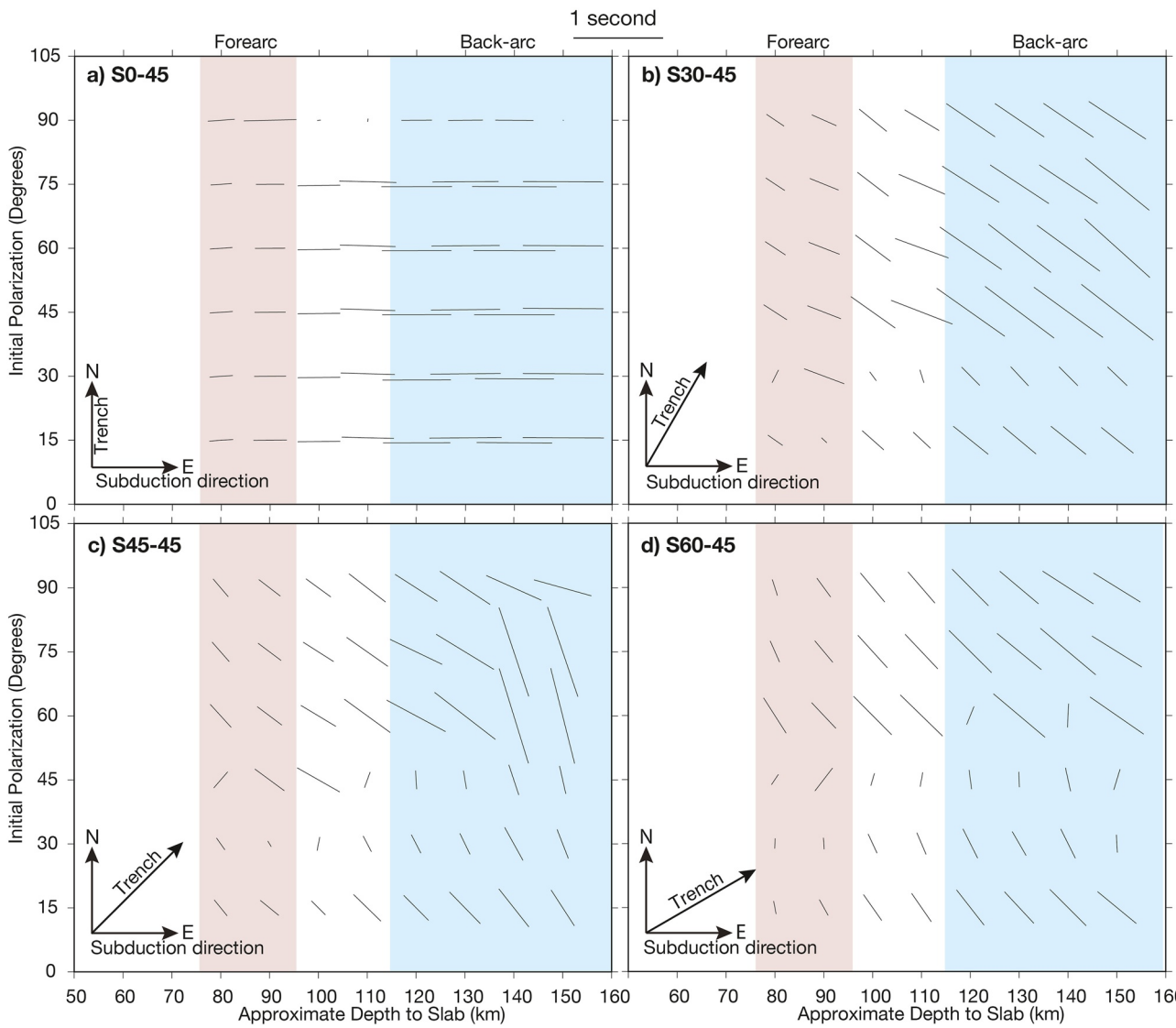

Figure 8. Possible shear wave splitting (SWS) parameters with depth to slab for various initial polarizations (15°–90° in 15° increments) in the (a) S0-45, (b) S30-45, (c) S45-45, and (d) S60-45 multilayer models. Bars in plot a have been shifted vertically to eliminate overlap. Red and blue shaded areas denote the forearc and the backarc regions, respectively, with the arc region located between them. See the main text regarding the likely overestimation of delay times for initial polarizations of 60° and 75° in subplot (c).

short delay times (e.g., 0.13s). If only off-peak fast directions are to be measured in real observations, they may give the impression that the medium below is not strongly anisotropic. Model S30-45, with less obliquity, shows only margin-normal fast directions in the arc region. The models with more obliquity (Models S45–45 and S60-45) result in margin-parallel or margin-oblique fast directions, respectively, in addition to margin-normal fast directions. In the arc region, both the margin-parallel and margin-oblique fast directions have smaller delay times (~0.15s), than the margin-normal fast directions (~0.15–0.7s) as the latter are generally associated with the PDT. Model S30-45 shows only margin-normal fast directions in the backarc region, like in the arc region. However, for the initial polarization directions that we tested, larger obliquity results in only margin-normal and margin-oblique fast directions in the backarc. The delay times for the margin-normal fast direction vary greatly (0.3–1s) but are in large part longer than those in the forearc and arc regions. The margin-oblique fast directions have smaller delay times than the margin-normal fast directions in the backarc with the exception of a few margin-oblique fast directions with >1 s delay time that are likely overestimated due to cycle skipping.

4. Discussion

Our CPO calculation results indicate that the fast axis does not always align with the mantle flow vector in 3-D flow due to oblique subduction. This is consistent with previous numerical work that performed FSE, ISA or CPO calculations for complex mantle flow patterns (e.g., Faccenda & Capitanio, 2013; Hall et al., 2000; Hu et al., 2017; Jadamec, 2016; Jadamec & Billen, 2010; Li et al., 2014), and as discussed earlier, the assumption that the fast axis is parallel to the flow direction is not appropriate for regions where the mantle flow direction changes quickly.

In this study, the SWS calculations are performed for *S* waves with a relatively high frequency that is suitable for local *S* waves, to which the contribution from the material below the mantle wedge is much smaller than SKS waves. Further, the given the vertical dimension of the mantle wedge beneath the forearc and the arc, the shorter wavelengths of the local *S* waves are more likely to resolve the vertical variation in anisotropy. Many previous numerical studies that calculate both the CPO distribution and SWS parameters for subduction zones aim to address larger-scale mantle flow patterns and assume SKS waves (e.g., Faccenda & Capitanio, 2013; Hu et al., 2017). Their calculations typically produce single set of SWS parameters for a given location through some averaging from multiple waves, and the calculated fast direction is generally consistent with the predominant orientation of fast axes in the medium that the waves travel through. In this study, we incorporate variations in the mantle flow and CPO at a finer scale to resolve the impact of seismic anisotropy in a relatively small region on the SWS parameters. There are generally at least two predominant fast axis orientations within a vertical column that are associated with mantle inflow and outflow. Our modeling results indicate that over the full range of initial polarization, a wide range of fast directions can result from the mantle wedge flow in oblique subduction zones, compared to normal subduction.

Our modeling results show that 3-D mantle wedge flow due to oblique subduction can also results in margin-normal fast directions that cannot be distinguished from those that result from 2-D flow patterns (i.e., margin-normal flow). An SWS study that uses local *S* waves for the Alaska subduction zone, for example, indicates margin-parallel fast direction above the cold mantle wedge nose and predominantly margin-normal fast directions with some variability in the arc and backarc regions (Richards et al., 2021). Another local SWS study on the Sumatra subduction zone indicates margin-parallel fast directions in the arc region and the margin-normal fast directions in the backarc (Collings et al., 2013). In our study, we do not model CPO or SWS through the cold mantle wedge nose, where olivine CPO may not be the main cause of seismic anisotropy, and therefore we do not have results to compare with these observations. In Sumatra, the margin-parallel fast direction is attributed to a strike-slip fault system (Collings et al., 2013). In both subduction zones, the delay times that are associated with margin-normal fast directions increase with the thickness of the mantle wedge, and these observations have been interpreted to indicate a 2-D mantle wedge flow (Collings et al., 2013; Richards et al., 2021). However, the subduction direction in these two regions is oblique to the margin, and the margin-normal fast directions and increasing delay times with the mantle wedge thickness are consistent with the SWS results for 3-D mantle wedge flow patterns due to oblique subduction.

Given the wide range of fast directions that can result in oblique subduction zones, the SWS observation at a station from a single earthquake event is difficult to interpret in terms of the mantle flow pattern and the anisotropy structure. It cannot be known for certain if the observation represents the PDT, SDT or an off-peak fast direction without the knowledge of the distribution of SWS with initial polarization. Even if there are a large number of observations, if the initial polarization directions all fall within a relatively narrow range, the SWS observations would be biased toward having a certain fast direction and delay time. Thus, availability of shear waves with a range of initial polarization to map out the full distribution of SWS parameters is critical to the interpretation of the results for oblique subduction zones.

As discussed in Section 1, margin-parallel fast directions are commonly observed in the forearc and arc regions regardless of subduction obliquity. Our analyses indicate that in the forearc and arc regions of oblique subduction zones, there are a wider range of initial polarizations that result in a margin-normal fast direction than in a margin-parallel fast direction (Figures 7 and 8). It is possible that the fast direction can be biased toward being margin-parallel in the forearc or arc at a particular station or even a particular oblique subduction zone due to the distribution of initial polarization. However, such bias is unlikely to occur consistently across subduction zones and would not explain the commonly observed margin-parallel fast directions.

To assess whether SWS observations are biased, one could compare the distribution of the observed SWS parameters with those presented in this study by producing the azimuthal polar plots that are introduced here. When the SWS parameters appear narrowly distributed, it may indicate a narrow range of initial polarization or insufficient observations. If there are sufficient observations with a wide range of observations, PDT and SDT can be identified, which can help to constrain the anisotropy structure. Although the delay times do generally increase from forearc to the backarc region in oblique subduction models, reflecting the increasing thickness of the anisotropic medium, they do not follow this trend for some initial polarization directions (Figure 8). This may explain why in some oblique subduction zones the delay time does not increase with the mantle wedge thickness (e.g., Levin et al., 2004). If there are sufficient data for statistical evaluations, such as in NE Japan (e.g., Nakajima & Hasegawa, 2004), it might be possible to observe the correlation between the delay time and the mantle wedge thickness. However, our models do not include the effects of an evolving subducting slab, along-strike variation in slab geometry, and other three-dimensional effects, and therefore the spatial variation in the observed SWS parameters is likely more complex than predicted by our calculations.

Our SWS calculations also indicate that even if the mantle wedge is highly anisotropic, due to the variation in the fast axis orientation along the raypath, the resulting SWS observations may not be indicative of strong anisotropy. This occurs because wavelets can interfere destructively through the medium, particularly in the forearc and arc regions as presented above, and also with the material above or below the mantle wedge. Consistently significant SWS or SWS with larger delay times may indicate sources of anisotropy besides the olivine CPO in the mantle wedge, such as the CPO and shape-preferred orientations in the overriding crust (Uchida et al., 2020), the hydrated or partially molten part of the mantle wedge (e.g., Holtzman et al., 2003; Katayama et al., 2009), and the subslab mantle.

5. Conclusions

Using model-predicted 3-D mantle wedge flow fields, we calculate the CPO of the olivine-enstatite aggregate using D-Rex for a suite of generic, kinematic-dynamic subduction models with varying obliquity and dip for both A-type and E-type CPO. In contrast to normal subduction, oblique subduction results in spatial variation of the flow direction and the fast axis; the flow is largely margin-normal in the inflow region, margin-parallel in the transition region, and parallel to the subduction direction in the outflow region. We find that there are only modest differences in the distribution of the fast axis orientation between A-type and E-type CPO, and we focus on A-type. The fast axes of mineral aggregates are generally subparallel to the mantle flow direction in the inflow region but become significantly misaligned with the flow direction in the transition region and remain slightly offset in the outflow region. The results are in agreement with the previous work that show the assumption that the fast axis aligns with the flow direction is not appropriate for regions where the mantle flow direction changes rapidly.

In the SWS calculations, we use the predicted distribution of olivine CPO in the mantle wedge. We find that SWS parameters are highly dependent on the initial polarization and when they are plotted on an azimuth polar plot,

their distribution changes from highly bimodal in the forearc and arc regions, which are more relaxed with larger obliquity, to less bimodal in the backarc with the range of fast directions that is more dependent on subduction obliquity. Off-peak delay times vary in magnitudes and may be too small to be resolvable in some forearc and arc locations. The majority of initial polarizations in the forearc and arc regions result in the margin-normal fast direction, but margin-parallel fast directions are also present. Fast directions in the backarc are limited to margin-normal and margin-oblique orientations and generally have longer delay times than in the forearc and arc regions.

For oblique subduction models, there is considerable variation in the fast direction which ranges from margin-normal to margin-parallel and in the delay times which range from null to >1 s. Due to the wide range of fast directions and delay times that result from a dependence on initial polarization, a single SWS measurement cannot be used to constrain the mantle wedge CPO or mantle wedge flow in an oblique subduction zone. Observations from shear waves with a wide range of initial polarizations are required to interpret SWS parameters at oblique subduction zones and to compare them to our plotted distributions. However, across all multilayer oblique subduction models, a wider range of initial polarization results in the margin-normal fast direction than in the margin-parallel fast direction, and the delay time increases with the thickness of the mantle wedge, adequately explaining the local SWS observations in the backarc for some oblique subduction zones. Our results also indicate that margin-parallel fast directions can result from olivine CPO in oblique subduction zones if initial polarizations happen to fall in a particular range. However, this is unlikely to explain the commonly observed margin-parallel fast directions in many oblique and normal subduction zones. With unconstrained variations in the initial polarization and the incidence angle and uncertainties in the CPO distribution, the interpretation of SWS parameters remains challenging.

Data Availability Statement

The main codes for this work are modified from D-Rex (Kaminski et al., 2004) and MATLAB Seismic Anisotropy Toolkit (Walker & Wookey, 2012). Some figures and plots are generated using Generic Mapping Tools (Wessel et al., 2013). The codes for this paper are preserved in Zenodo as Kenyon and Wada (2022) and can be found at https://doi.org/10.5281/zenodo.5842726.

Acknowledgments
We thank Phil Skemer and an anonymous reviewer for their constructive comments that helped to improve the manuscript. We thank Maximiliano Bezada, Neala Creasy, Karen Fischer, Lars Hansen, and Zachary Michel, for discussions during the early phase of this research. This research was partially funded by the National Science Foundation through Grant EAR-1620604 to I.W. and the University of Minnesota—Twin Cities through startup funds. The details of the model and additional modeling results that are discussed in this article are found in Supporting Information, and the modified version of D-Rex and the SWS calculation code are available on Zenodo. Figures were generated using the Generic Mapping Tool and MSAT.

References

Abramson, E. H., Brown, J. M., Slutsky, L. J., & Zaug, J. (1997). The elastic constants of San Carlos olivine to 17 GPa. *Journal of Geophysical Research*, *102*(B6), 12253–12263. https://doi.org/10.1029/97JB00682

Abt, D. L., & Fischer, K. M. (2008). Resolving three-dimensional anisotropic structure with shear wave splitting tomography. *Geophysical Journal International*, *173*(3), 859–886. https://doi.org/10.1111/j.1365-246X.2008.03757.x

Abt, D. L., Fischer, K. M., Abers, G. A., Protti, M., González, V., & Strauch, W. (2010). Constraints on upper mantle anisotropy surrounding the Cocos slab from SK (K) S splitting. *Journal of Geophysical Research*, *115*, B06316. https://doi.org/10.1029/2009JB006710

Abt, D. L., Fischer, K. M., Abers, G. A., Strauch, W., Protti, J. M., & González, V. (2009). Shear wave anisotropy beneath Nicaragua and Costa Rica: Implications for flow in the mantle wedge. *Geochemistry, Geophysics, Geosystems*, *10*, Q05S15. https://doi.org/10.1029/2009GC002375

Aragon, J. C., Long, M. D., & Benoit, M. H. (2017). Lateral variations in SKS splitting across the MAGIC array, central Appalachians. *Geochemistry, Geophysics, Geosystems*, *18*, 4136–4155. https://doi.org/10.1002/2017GC007169

Babuska, V., & Cara, M. (1991). *Seismic anisotropy in the Earth*. Dordrecht, The Netherlands: Kluwer Academic Publishers.

Becker, T. W., Chevrot, S., Schulte-Pelkum, V., & Blackman, D. K. (2006). Statistical properties of seismic anisotropy predicted by upper mantle geodynamic models. *Journal of Geophysical Research*, *111*, B08309. https://doi.org/10.1029/2005JB004095

Bengtson, A. K., & van Keken, P. E. (2012). Three-dimensional thermal structure of subduction zones: Effects of obliquity and curvature. *Solid Earth*, *3*(2), 365–373. https://doi.org/10.5194/se-3-365-2012

Bezacier, L., Reynard, B., Bass, J. D., Sanchez-Valle, C., & Van de Moortèle, B. (2010). Elasticity of antigorite, seismic detection of serpentinites, and anisotropy in subduction zones. *Earth and Planetary Science Letters*, *289*(1–2), 198–208. https://doi.org/10.1016/j.epsl.2009.11.009

Boneh, Y., Morales, L. F. G., Kaminski, E., & Skemer, P. (2015). Modeling olivine CPO evolution with complex deformation histories: Implications for the interpretation of seismic anisotropy in the mantle. *Geochemistry, Geophysics, Geosystems*, *16*, 3436–3455. https://doi.org/10.1002/2015GC005964

Boneh, Y., & Skemer, P. (2014). The effect of deformation history on the evolution of olivine CPO. *Earth and Planetary Science Letters*, *406*, 213–222. https://doi.org/10.1016/j.epsl.2014.09.018

Bonnin, M., Tommasi, A., Hassani, R., Chevrot, S., Wookey, J., & Barruol, G. (2012). Numerical modelling of the upper-mantle anisotropy beneath a migrating strike-slip plate boundary: The San Andreas fault system. *Geophysical Journal International*, *191*(2), 436–458. https://doi.org/10.1111/j.1365-246X.2012.05650.x

Browaeys, J. T., & Chevrot, S. (2004). Decomposition of the elastic tensor and geophysical applications. *Geophysical Journal International*, *159*(2), 667–678. https://doi.org/10.1111/j.1365-246X.2004.02415.x

Chevrot, S. (2000). Multichannel analysis of shear wave splitting. *Journal of Geophysical Research*, *105*(B9), 21579–21590. https://doi.org/10.1029/2000JB900199

Christensen, N. I. (1984). The magnitude, symmetry and origin of upper mantle anisotropy based on fabric analyses of ultramafic tectonites. *Geophysical Journal International*, *76*(1), 89–111. https://doi.org/10.1111/j.1365-246X.1984.tb05025.x

Collings, R., Rietbrock, A., Lange, D., Tilmann, F., Nippress, S., & Natawidjaja, D. (2013). Seismic anisotropy in the Sumatra subduction zone. *Journal of Geophysical Research: Solid Earth*, *118*, 5372–5390. https://doi.org/10.1002/jgrb.50157

Confal, J. M., Faccenda, M., Eken, T., & Taymaz, T. (2018). Numerical simulation of 3-D mantle flow evolution in subduction zone environments in relation to seismic anisotropy beneath the eastern Mediterranean region. *Earth and Planetary Science Letters*, *497*, 50–61. https://doi.org/10.1016/j.epsl.2018.06.005

Currie, C. A., Wang, K., Hyndman, R. D., & He, J. (2004). The thermal effects of steady-state slab-driven mantle flow above a subducting plate: The Cascadia subduction zone and backarc. *Earth and Planetary Science Letters*, *223*(1–2), 35–48. https://doi.org/10.1016/j.epsl.2004.04.020

England, P. C., & Katz, R. F. (2010). Melting above the anhydrous solidus controls the location of volcanic arcs. *Nature*, *467*(7316), 700–703. https://doi.org/10.1038/nature09417

Faccenda, M., & Capitanio, F. A. (2013). Seismic anisotropy around subduction zones: Insights from three-dimensional modeling of upper mantle deformation and SKS splitting calculations. *Geochemistry, Geophysics, Geosystems*, *14*, 243–262. https://doi.org/10.1002/ggge.20055

Funiciello, F., Moroni, M., Piromallo, C., Faccenna, C., Cenedese, A., & Bui, H. A. (2006). Mapping mantle flow during retreating subduction: Laboratory models analyzed by feature tracking. *Journal of Geophysical Research*, *111*, B03402. https://doi.org/10.1029/2005JB003792

Furukawa, Y. (1993). Depth of the decoupling plate interface and thermal structure under arcs. *Journal of Geophysical Research*, *98*(B11), 20005–20013. https://doi.org/10.1029/93JB02020

Greve, S. M., & Savage, M. K. (2009). Modelling seismic anisotropy variations across the Hikurangi subduction margin, New Zealand. *Earth and Planetary Science Letters*, *285*(1–2), 16–26. https://doi.org/10.1016/j.epsl.2009.05.035

Greve, S. M., Savage, M. K., & Hofmann, S. D. (2008). Strong variations in seismic anisotropy across the Hikurangi subduction zone, North Island, New Zealand. *Tectonophysics*, *462*(1–4), 7–21. https://doi.org/10.1016/j.tecto.2007.07.011

Hall, C. E., Fischer, K. M., Parmentier, E. M., & Blackman, D. K. (2000). The influence of plate motions on three-dimensional back arc mantle flow and shear wave splitting. *Journal of Geophysical Research*, *105*(B12), 28009–28033. https://doi.org/10.1029/2000JB900297

Hirth, G., & Kohlstedt, D. L. (2003). Rheology of the upper mantle and the mantle wedge: A view from the experimentalists. In J.Eiler (Ed.), *Inside the subduction facotry* (pp. 83–105). Washington, DC: Amerian Geophysical Union. https://doi.org/10.1029/138GM06

Hoernle, K., Abt, D. L., Fischer, K. M., Nichols, H., Hauff, F., Abers, G. A., et al. (2008). Arc-parallel flow in the mantle wedge beneath Costa Rica and Nicaragua. *Nature*, *451*(7182), 1094–1097. https://doi.org/10.1038/nature06550

Holtzman, B. K., Kohlstedt, D. L., Zimmerman, M. E., Heidelbach, F., Hiraga, T., & Hustoft, J. (2003). Melt segregation and strain Partitioning: Implications for seismic anisotropy and mantle flow. *Science*, *301*(5637), 1227–1230. https://doi.org/10.1126/science.1087132

Horn, C., Bouilhol, P., & Skemer, P. (2020). Serpentinization, deformation, and seismic anisotropy in the subduction mantle wedge. *Geochemistry, Geophysics, Geosystems*, *21*, e2020GC008950. https://doi.org/10.1029/2020GC008950

Hu, J., Faccenda, M., & Liu, L. (2017). Subduction-controlled mantle flow and seismic anisotropy in South America. *Earth and Planetary Science Letters*, *470*, 13–24. https://doi.org/10.1016/j.epsl.2017.04.027

Jadamec, M. A. (2016). Insights on slab-driven mantle flow from advances in three-dimensional modelling. *Journal of Geodynamics*, *100*, 51–70. https://doi.org/10.1016/j.jog.2016.07.004

Jadamec, M. A., & Billen, M. I. (2010). Reconciling surface plate motions with rapid three-dimensional mantle flow around a slab edge. *Nature*, *465*(7296), 338–341. https://doi.org/10.1038/nature09053

Jadamec, M. A., & Billen, M. I. (2012). The role of rheology and slab shape on rapid mantle flow: Three-dimensional numerical models of the Alaska slab edge. *Journal of Geophysical Research*, *117*, B02304. https://doi.org/10.1029/2011JB008563

Ji, Y., & Yoshioka, S. (2015). Effects of slab geometry and obliquity on the interplate thermal regime associated with the subduction of three-dimensionally curved oceanic plates. *Geoscience Frontiers*, *6*(1), 61–78. https://doi.org/10.1016/j.gsf.2014.04.011

Kaminski, E., & Okaya, D. A. (2018). How to detect water in the mantle wedge of a subduction zone using seismic anisotropy. *Geophysical Research Letters*, *45*, 13298–13305. https://doi.org/10.1029/2018GL079571

Kaminski, E., Ribe, N. M., & Browaeys, J. T. (2004). D-Rex, a program for calculation of seismic anisotropy due to crystal lattice preferred orientation in the convective upper mantle. *Geophysical Journal International*, *158*(2), 744–752. https://doi.org/10.1111/j.1365-246X.2004.02308.x

Karato, S., Jung, H., Katayama, I., & Skemer, P. (2008). Geodynamic significance of seismic anisotropy of the upper mantle: New insights from laboratory studies. *Annual Review of Earth and Planetary Sciences*, *36*(1), 59–95. https://doi.org/10.1146/annurev.earth.36.031207.124120

Katayama, I., Hirauchi, K. I., Michibayashi, K., & Ando, J. I. (2009). Trench-parallel anisotropy produced by serpentine deformation in the hydrated mantle wedge. *Nature*, *461*(7267), 1114–1117. https://doi.org/10.1038/nature08513

Kenyon, L. M., & Wada, I. (2022). Package for calculating crystal preferred orientation and local shear wave splitting for 3-D mantle wedge flow in subduction zones. *Zenodo*. https://doi.org/10.5281/zenodo.5842726

Kincaid, C., & Griffiths, R. W. (2004). Variability in flow and temperatures within mantle subduction zones. *Geochemistry, Geophysics, Geosystems*, *5*, Q06002. https://doi.org/10.1029/2003GC000666

Kneller, E. A., & van Keken, P. E. (2007). Trench-parallel flow and seismic anisotropy in the Mariana and Andean subduction systems. *Nature*, *450*(7173), 1222–1225. https://doi.org/10.1038/nature06429

Kneller, E. A., & van Keken, P. E. (2008). Effect of three-dimensional slab geometry on deformation in the mantle wedge: Implications for shear wave anisotropy. *Geochemistry, Geophysics, Geosystems*, *9*, Q01003. https://doi.org/10.1029/2007GC001677

Levin, V., Droznin, D., Park, J., & Gordeev, E. (2004). Detailed mapping of seismic anisotropy with local shear waves in southeastern Kamchatka. *Geophysical Journal International*, *158*(3), 1009–1023. https://doi.org/10.1111/j.1365-246X.2004.02352.x

Li, Z., Di Leo, J. F., & Ribe, N. M. (2014). Subduction-induced mantle flow, finite strain, and seismic anisotropy: Numerical modeling. *Journal of Geophysical Research: Solid Earth*, *119*, 5052–5076. https://doi.org/10.1002/2014JB010996

Long, M. D., & Becker, T. W. (2010). Mantle dynamics and seismic anisotropy. *Earth and Planetary Science Letters*, *297*(3–4), 341–354. https://doi.org/10.1016/j.epsl.2010.06.036

Long, M. D., & Silver, P. G. (2008). The subduction zone flow field from seismic anisotropy: A global view. *Science*, *319*(5861), 315–318. https://doi.org/10.1126/science.1150809

Long, M. D., & Wirth, E. A. (2013). Mantle flow in subduction systems: The mantle wedge flow field and implications for wedge processes. *Journal of Geophysical Research: Solid Earth*, *118*, 583–606. https://doi.org/10.1002/jgrb.50063

MacDougall, J. G., Jadamec, M. A., & Fischer, K. M. (2017). The zone of influence of the subducting slab in the asthenospheric mantle. *Journal of Geophysical Research: Solid Earth*, *122*, 6599–6624. https://doi.org/10.1002/2017JB014445

McPherson, A. M., Christensen, D. H., Abers, G. A., & Tape, C. (2020). Shear wave splitting and mantle flow beneath Alaska. *Journal of Geophysical Research: Solid Earth*, *125*, e2019JB018329. https://doi.org/10.1029/2019JB018329

Menke, W., & Levin, V. (2003). The cross-convolution method for interpreting SKS splitting observations, with application to one and two-layer anisotropic Earth models. *Geophysical Journal International*, *154*(2), 379–392. https://doi.org/10.1046/j.1365-246X.2003.01937.x

Michibayashi, K., Mainprice, D., Fujii, A., Uehara, S., Shinkai, Y., Kondo, Y., et al. (2016). Natural olivine crystal-fabrics in the Western Pacific convergence region: A new method to identify fabric type. *Earth and Planetary Science Letters*, *443*, 70–80. https://doi.org/10.1016/j.epsl.2016.03.019

Molnar, P., & England, P. (1990). Temperatures, heat flux, and frictional stress near major thrust faults. *Journal of Geophysical Research*, *95*(B4), 4833–4856. https://doi.org/10.1029/JB095iB04p04833

Nagaya, T., Walker, A. M., Wookey, J., Wallis, S. R., Ishii, K., & Kendall, J. M. (2016). Seismic evidence for flow in the hydrated mantle wedge of the Ryukyu subduction zone. *Scientific Reports*, *6*(1), 29981. https://doi.org/10.1038/srep29981

Nakajima, J., & Hasegawa, A. (2004). Shear-wave polarization anisotropy and subduction-induced flow in the mantle wedge of northeastern Japan. *Earth and Planetary Science Letters*, *225*(3–4), 365–377. https://doi.org/10.1016/j.epsl.2004.06.011

Plunder, A., Thieulot, C., & van Hinsbergen, D. J. J. (2018). The effect of obliquity on temperature in subduction zones: Insights from 3-D numerical modeling. *Solid Earth*, *9*(3), 759–776. https://doi.org/10.5194/se-9-759-2018

Reynard, B. (2013). Serpentine in active subduction zones. *Lithos*, *178*, 171–185. https://doi.org/10.1016/j.lithos.2012.10.012

Richards, C., Tape, C., Abers, G. A., & Ross, Z. E. (2021). Anisotropy variations in the Alaska subduction zone based on shear-wave splitting from Intraslab earthquakes. *Geochemistry, Geophysics, Geosystems*, *22*, e2020GC009558. https://doi.org/10.1029/2020GC009558

Rümpker, G., & Silver, P. G. (1998). Apparent shear-wave splitting parameters in the presence of vertically varying anisotropy. *Geophysical Journal International*, *135*(3), 790–800. https://doi.org/10.1046/j.1365-246X.1998.00660.x

Savage, M. K. (1999). Seismic anisotropy and mantle deformation: What have we learned from shear wave splitting? *Reviews of Geophysics*, *37*(1), 65–106. https://doi.org/10.1029/98RG02075

Schellart, W. P. (2004). Kinematics of subduction and subduction-induced flow in the upper mantle. *Journal of Geophysical Research*, *109*, B07401. https://doi.org/10.1029/2004JB002970

Silver, P. G. (1996). Seismic anisotropy beneath the continents: Probing the depths of geology. *Annual Review of Earth and Planetary Sciences*, *24*, 385–432. https://doi.org/10.1146/annurev.earth.24.1.385

Silver, P. G., & Chan, W. W. (1991). Shear wave splitting and subcontinental mantle deformation. *Journal of Geophysical Research*, *96*(B10), 16429–16454. https://doi.org/10.1029/91JB00899

Skemer, P., & Hansen, L. N. (2016). Inferring upper-mantle flow from seismic anisotropy: An experimental perspective. *Tectonophysics*, *668–669*, 1–14. https://doi.org/10.1016/j.tecto.2015.12.003

Skemer, P., Warren, J. M., & Hirth, G. (2012). The influence of deformation history on the interpretation of seismic anisotropy. *Geochemistry, Geophysics, Geosystems*, *13*, Q03006. https://doi.org/10.1029/2011GC003988

Stein, C. A., & Stein, S. (1992). A model for the global variation in oceanic depth and heat flow with lithospheric age. *Nature*, *359*(6391), 123–129. https://doi.org/10.1038/359123a0

Syracuse, E. M., van Keken, P. E., & Abers, G. A. (2010). The global range of subduction zone thermal models. *Physics of the Earth and Planetary Interiors*, *183*(1–2), 73–90. https://doi.org/10.1016/j.pepi.2010.02.004

Uchida, N., Nakajima, J., Wang, K., Takagi, R., Yoshida, K., Nakayama, T., et al. (2020). Stagnant forearc mantle wedge inferred from mapping of shear-wave anisotropy using S-net seafloor seismometers. *Nature Communications*, *11*(1), 5676. https://doi.org/10.1038/s41467-020-19541-y

van Keken, P. E., Kiefer, B., & Peacock, S. M. (2002). High-resolution models of subduction zones: Implications for mineral dehydration reactions and the transport of water into the deep mantle. *Geochemistry, Geophysics, Geosystems*, *3*(10), 1056. https://doi.org/10.1029/2001GC000256

van Keken, P. E., Wada, I., Sime, N., & Abers, G. A. (2019). Thermal structure of the forearc in subduction zones: A comparison of methodologies. *Geochemistry, Geophysics, Geosystems*, *20*, 3268–3288. https://doi.org/10.1029/2019GC008334

Wada, I. (2021). A simple picture of mantle wedge flow patterns and temperature variation. *Journal of Geodynamics*, *146*, 101848. https://doi.org/10.1016/j.jog.2021.101848

Wada, I., He, J., Hasegawa, A., & Nakajima, J. (2015). Mantle wedge flow pattern and thermal structure in Northeast Japan: Effects of oblique subduction and 3-D slab geometry. *Earth and Planetary Science Letters*, *426*, 76–88. https://doi.org/10.1016/j.epsl.2015.06.021

Wada, I., & Wang, K. (2009). Common depth of slab-mantle decoupling: Reconciling diversity and uniformity of subduction zones. *Geochemistry, Geophysics, Geosystems*, *10*,Q10009. https://doi.org/10.1029/2009GC002570

Walker, A. M., & Wookey, J. (2012). MSAT—A new toolkit for the analysis of elastic and seismic anisotropy. *Computers & Geosciences*, *49*, 81–90. https://doi.org/10.1016/j.cageo.2012.05.031

Walsh, E., Arnold, R., & Savage, M. K. (2013). Silver and Chan revisited. *Journal of Geophysical Research: Solid Earth*, *118*, 5500–5515. https://doi.org/10.1002/jgrb.50386

Wessel, P., Smith, W. H. F., Scharroo, R., Luis, J., & Wobbe, F. (2013). Generic mapping tools: Improved version released. *EOS, Transactions American Geophysical Union*, *94*(45), 409–410. https://doi.org/10.1002/2013EO450001

Wirth, E., & Long, M. D. (2010). Frequency-dependent shear wave splitting beneath the Japan and Izu-Bonin subduction zones. *Physics of the Earth and Planetary Interiors*, *181*(3–4), 141–154. https://doi.org/10.1016/j.pepi.2010.05.006

Zhang, S., & Karato, S. (1995). Lattice preferred orientation of olivine aggregates deformed in simple shear. *Nature*, *375*, 774–777. https://doi.org/10.1038/375774a0

Zhou, Q., Hu, J., Liu, L., Chaparro, T., Stegman, D. R., & Faccenda, M. (2018). Western U.S. seismic anisotropy revealing complex mantle dynamics. *Earth and Planetary Science Letters*, *500*, 156–167. https://doi.org/10.1016/j.epsl.2018.08.015

References From the Supporting Information

Anderson, O. L., & Isaak, D. G., (1995). Elastic constants of mantle minerals at high temperature. In T. J. Ahrens (Ed.), *Mineral physical and crystallography, A handbook of physical constants* (pp. 64–97). Washington, DC: Amerian Geophysical Union. https://doi.org/10.1029/RF002p0064

Mainprice, D. (2007). Seismic anisotropy of the deep Earth from a mineral and rock physics perspective. *Treatise on Geophysics*, *2*, 437–491. https://doi.org/10.1016/B978-044452748-6.00045-6

Silver, P. G., & Savage, M. K. (1994). The interpretation of shear-wave splitting parameters in the presence of two anisotropic layers. *Geophysical Journal International*, *119*(3), 949–963. https://doi.org/10.1111/j.1365-246X.1994.tb04027.x

Weidner, D. J., Wang, H., & Ito, J. (1978). Elasticity of orthoenstatite. *Physics of the Earth and Planetary Interiors*, *17*(2), P7–P13. https://doi.org/10.1016/0031-9201(78)90043-2